

Article

# Design of Perovskite-Type Fluorides Cathodes for Na-ion Batteries: Correlation between Structure and Transport

**Michele Montalbano** <sup>1</sup>, **Daniele Callegari** <sup>1,2</sup> , **Umberto Anselmi Tamburini** <sup>1,2</sup> and **Cristina Tealdi** <sup>1,2,\*</sup> <sup>1</sup> Department of Chemistry, University of Pavia, 27100 Pavia, Italy<sup>2</sup> National Reference Centre for Electrochemical Energy Storage (GISEL)-INSTM UdR Pavia, 27100 Pavia, Italy

\* Correspondence: cristina.tealdi@unipv.it

**Abstract:** Transition metal-based sodium fluoro-perovskite of general formula  $\text{NaMF}_3$  ( $\text{M} = \text{Fe}, \text{Mn}$ , and  $\text{Co}$ ) were investigated as cathode materials for rechargeable Na-ion batteries. Preliminary results indicated Na-ion reversible intercalation but highlighted the need to find optimization strategies to improve conductivity and to modulate the operating voltages within experimentally accessible electrolytes' stability windows, in order to fully exploit their potential as high-voltage cathodes. In this study, we combined experimental and computational techniques to investigate structures, defects, and intercalation properties of the  $\text{NaFe}_{1-x}\text{Mn}_x\text{F}_3$  and  $\text{NaCo}_{1-x}\text{Mn}_x\text{F}_3$  systems. Through the use of a simple solvothermal synthesis, we demonstrated the possibility to modulate the sample's morphology in order to obtain fine and dispersed powder samples. The structural results indicated the formations of two solid solutions with a perovskite structure over the entire compositional range investigated. Atomistic simulations suggested that Na-ion diffusion in these systems was characterized by relatively high migration barriers and it was likely to follow three-dimensional paths, thus limiting the effect of anti-site defects. The correlation between structural and computational data highlighted the possibility to modulate both ionic and electronic conductivity as a function of the composition.

**Keywords:** Na-ion battery; perovskite structure; high-voltage cathode; fluoride ion; solid solution; atomistic modeling; X-ray diffraction; Na-ion diffusion



**Citation:** Montalbano, M.; Callegari, D.; Anselmi Tamburini, U.; Tealdi, C. Design of Perovskite-Type Fluorides Cathodes for Na-ion Batteries: Correlation between Structure and Transport. *Batteries* **2022**, *8*, 126. <https://doi.org/10.3390/batteries8090126>

Academic Editors: Seung-Tae Hong and Matthieu Dubarry

Received: 14 July 2022

Accepted: 2 September 2022

Published: 13 September 2022

**Publisher's Note:** MDPI stays neutral with regard to jurisdictional claims in published maps and institutional affiliations.



**Copyright:** © 2022 by the authors. Licensee MDPI, Basel, Switzerland. This article is an open access article distributed under the terms and conditions of the Creative Commons Attribution (CC BY) license (<https://creativecommons.org/licenses/by/4.0/>).

## 1. Introduction

The growing use of renewable energies and electrical vehicles, as well as the demand for portable electronics, drives the development of novel materials and technologies for rechargeable batteries. Li-ion batteries (LIBs) have been the technology of choice for decades, but the interest in alternative chemistries is constantly growing based on the necessity to meet the future market's requests. Different applications pose different requirements in terms of the energy stored, specific or gravimetric capacity, stability over time, charging speed, and operating temperature. Being able to pick the most appropriate technology for the target application will be of great importance to optimize the use of primary resources, with particular attention to limit the use of critical raw materials to those market fields that cannot easily come to a compromise on their use [1].

In this scenario, Na-ion battery (NIB) technology is the most mature alternative to LIB technology [2]. Compared to  $\text{Li}^+$ ,  $\text{Na}^+$  is more abundant and evenly distributed. Although heavier and larger, the intercalation mechanisms and energetics for the two metal ions are similar and the device working principles are the same. This ensures that developments in materials and technologies for NIBs proceed faster than for LIBs, as the optimization process can benefit from decades of efforts in Li-ion technology.

The search for novel materials for NIBs is active, and the interest in finding optimal cathode materials is high, just as for LIBs. The main families studied as cathodes for NIBs are layered transition metal oxides, tunnel-structure Mn-based oxides, polyanionic

compounds (e.g., phosphates and fluorophosphates), and Prussian blue analogues [3,4]. Stable high-voltage cathode materials are desirable, as they will allow for higher energy densities. In this regard, transition metal-based sodium fluoro-perovskites of general formula  $\text{NaMF}_3$  ( $M = \text{Fe}, \text{Mn}$ , and  $\text{Co}$ ) have been proposed as valid candidates [5–9].

Calculated voltages as a function of  $x$  for  $\text{Na}_{1-x}\text{MF}_3$  ( $M = \text{Fe}, \text{Mn}$ , and  $\text{Co}$ ) based on density functional theory [5] predicted average operating voltages of 3.06 V, 4.10 V, and 4.61 V vs.  $\text{Na}^+/\text{Na}$  for  $M = \text{Fe}, \text{Mn}$ , and  $\text{Co}$ , respectively. The intercalation of Na ion proceeds through two voltage plateaus for Fe ( $x = 0.5$ ) and three voltage plateaus for Mn and Co ( $x = 0.5$  and 0.25, respectively). The high average operating voltage of  $\text{NaCoF}_3$  in particular and, to a lesser extent,  $\text{NaMnF}_3$  are very promising for high-voltage applications, but the possibility to make use of these compositions is limited by the electrolyte's stability window and large over-potentials, which allow exploiting only a portion of the available change in Na stoichiometry, thus resulting in poor specific capacities compared to the theoretical ones [5]. The electrochemical characterization of  $\text{NaFeF}_3$  has instead been reported by using conventional electrolytes such as 1 M  $\text{NaPF}_6$  in propylene carbonate (PC):fluoroethylene carbonate (FEC) [5], 1 M  $\text{NaClO}_4$  in PC [6,9], or 1 M  $\text{NaClO}_4$  in EC/DMC [8]. These studies confirm the potential of  $\text{NaFeF}_3$  as a cathode material for NIBs, reporting specific capacities higher than  $150 \text{ mAh g}^{-1}$ . They also highlight the strong dependency of such values from particle morphology and partial carbon coating, as frequently observed for cathode materials. In particular, nanosizing and carbon coatings are expected to pave the way for the application of  $\text{NaFeF}_3$  as a green and cost-effective cathode for NIBs [9], as this approach has been highly rewarding for several well-studied and commercial cathodes, such as  $\text{LiFePO}_4$  [10].

The perovskite structure offers a great versatility to accommodate various and wide substitutions, giving rise to the possibility to modulate the average operating voltage as well as the conductivity of the final compound based on chemical composition. With this background, we decided to investigate the preparation of the  $\text{NaFe}_{1-x}\text{Mn}_x\text{F}_3$  and  $\text{NaCo}_{1-x}\text{Mn}_x\text{F}_3$  systems. All the compositions were prepared through a simple solution reaction technique with the possibility to modulate the particles' average dimensions. The structural changes along with composition have been investigated through X-ray powder diffraction and the results correlated to the energetics of Na diffusion in these systems, investigated for the first time in this study through atomistic modeling techniques in order to shed light on the mechanism of Na intercalation in this novel family of cathode materials.

## 2. Materials and Methods

Powder samples of nominal composition  $\text{NaCo}_{1-x}\text{Mn}_x\text{F}_3$  ( $x = 1, 0.75, 0.5, 0.25$ , and 0) and  $\text{NaFe}_{1-x}\text{Mn}_x\text{F}_3$  ( $x = 1, 0.75, 0.5, 0.25$ , and 0) were prepared according to a simple and green procedure, in agreement with a previous report for the  $\text{NaCoF}_3$  composition [11]. Hydrated metal chlorides of the transition metal cations were dissolved in ethylene glycol; then, an aqueous solution of ammonium fluoride ( $\text{NH}_4\text{F}$ ) in an appropriate stoichiometric ratio was added. After 30 min, stoichiometric amounts of sodium acetate were added under vigorous stirring. The resultant solution was transferred to a Teflon-lined stainless-steel reactor and heated at  $200^\circ\text{C}$  for 12 h. For certain samples, 0.2–0.4 g of trisodium citrate dihydrate were added to the transition metal cation solution in ethylene glycol prior to the addition of the aqueous solution of ammonium fluoride to modulate the particles' size and aggregation state. For the Fe-containing samples, the synthesis was conducted in an Ar-filled glove box starting from carefully dehydrated chemical precursors, because, as shown in Figure S1 (ESI), the same synthetic procedure carried out in air favored the Fe oxidation from  $\text{Fe}^{2+}$  to  $\text{Fe}^{3+}$ , resulting in the formation of  $\text{Na}_3\text{FeF}_6$  impurities. After the thermal treatment, the particles were centrifuged at 6000 rpm for 20 min, and the deposited powders were washed with ethanol and further centrifuged twice before being dried at  $60^\circ\text{C}$  overnight.

The X-ray powder diffraction (XRPD) patterns of all the samples were acquired with a Bruker D8 Advance diffractometer in Bragg-Brentano geometry by using the  $\text{Cu-K}_\alpha$

radiation. For the structural characterization, acquisitions were performed in the  $2\theta$  range of 15–90 degrees with a fixed counting time of 8 s per step and a step size of 0.02 ( $2\theta$ ). Rietveld refinement analysis was carried out through the FullProf package [12]. Starting structural parameters were adopted from [13].

The as-prepared powders were graphite-coated and analyzed through scanning electron microscopy (SEM) using a TESCAN Mira 3 XMU instrument at an applied voltage of 15 kV and a magnification of 50 kx.

Energy minimization techniques based on atomistic simulations which relies on interatomic potentials methods, as embodied in the GULP code [14,15], were used to model the three compositions of  $\text{NaCoF}_3$ ,  $\text{NaFeF}_3$ , and  $\text{NaMnF}_3$ . The computational investigation was performed on the three end-member compositions and not on all of the mixed cation compositions due to the complexity of simulating such disordered systems, which would require large supercells in order to reproduce the stoichiometry as well as the experimental structural information that confirmed the long-range disorder of the mixed cations (see Section 3.1). The starting structural parameters were those derived in this study from Rietveld refinement and reported in Table S1 (ESI). The method requires the specification of an effective potential function, which expresses the total energy of the system as a function of the nuclear coordinates. In this study, short-range interactions were modeled using a Buckingham potential, which was defined as follows:

$$U(r) = Ae^{\frac{-r}{\rho}} - \frac{C}{r^6}, \quad (1)$$

where  $A$ ,  $\rho$ , and  $C$  are ion–ion adjustable parameters and  $r$  is the inter-atomic distance. The starting potential parameters were taken from a previous study on fluoride-containing cathode materials [16]. The complete set of potentials parameters used in this study is reported in Table S2 (ESI). The model includes electronic polarization with the use of the shell model [17], effective in reproducing the polarization induced by the presence of charged defects in the crystal. Defect formation energies and energy barriers for Na ion diffusion were modeled using the Mott–Littleton methodology [18], in which the crystal is partitioned in two concentric regions: the inner sphere around the defect, where ions relaxation is treated explicitly, and an external sphere extending to infinity, whereby ions positions are relaxed by quasi-continuum methods. For the present calculations, region 1 radius was set to 20 Å and included approximately 5000 ions, which was seen to give converged estimates of the defect formation and migration energies with respect to the region's size.

### 3. Results and Discussion

#### 3.1. Materials Synthesis and Characterization

Figure 1 shows the XRPD patterns of the three single cation compositions, i.e.,  $\text{NaFeF}_3$ ,  $\text{NaMnF}_3$ , and  $\text{NaCoF}_3$ , prepared without the addition of sodium citrate. The direct comparison with the corresponding calculated diffraction pattern (reported as vertical lines) indicated that the adopted synthesis strategy produced single-phase materials of these compositions. As expected, the compounds crystallized in the orthorhombic space group  $Pnma$  (n.62), with a perovskite structure composed of  $\text{MF}_6$  distorted and tilted octahedra [13], as shown in Figure 2. The structure is characterized by the presence of channels in which Na ions may preferentially diffuse along the  $b$  axis direction (Figure 2a) or within the  $ac$  plane (Figure 2b), with a hopping distance of approximately 4 Å, depending on the direction and the composition.

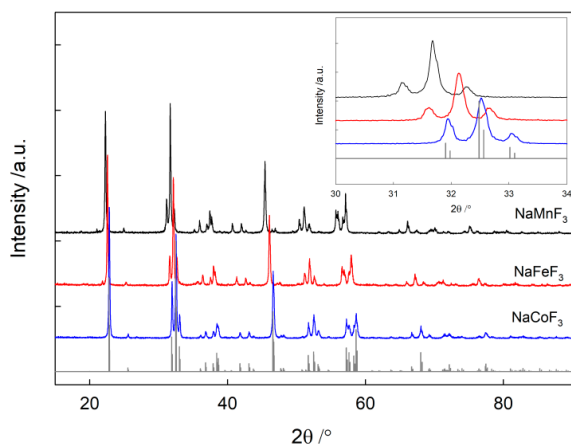


**Figure 1.** XRPD patterns of the  $\text{NaMF}_3$  samples ( $M = \text{Co, Fe, and Mn}$ ) prepared without sodium citrate. The vertical lines used for comparison ( $\text{NaCoF}_3$ ) were calculated based on the data reported in [13] (ICSD 98-007-2321).

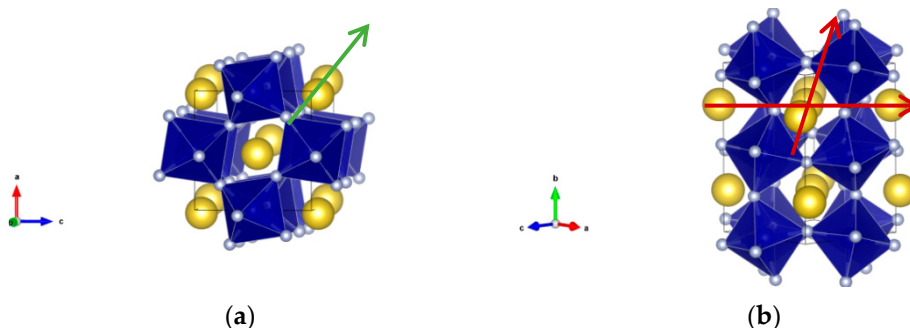


**Figure 2.** Crystal structures of  $\text{NaMF}_3$ , showing the presence of preferential diffusion paths for  $\text{Na}$  ion diffusion: (a) along the crystallographic axis  $b$  (green); and (b) within the  $ac$  plane (red).

Based on these XRPD measurements, the structural data for the three compositions were derived, which are summarized in Table S1 (ESI). Figure 3 shows the comparison between the experimental and Rietveld refined patterns of the  $\text{NaMnF}_3$  composition, selected as a representative example.

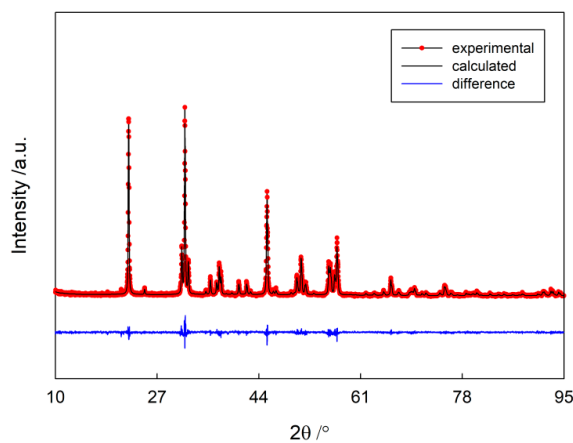


**Figure 3.** Rietveld refined XRPD pattern of the  $\text{NaMnF}_3$  sample (ICSD: 98-006-7745) prepared without sodium citrate ( $\chi^2 = 1.37$ ).

The XRPD patterns of the mixed metal cations samples were consistent with the formations of two solid solutions ( $\text{NaCo}_{1-x}\text{Mn}_x\text{F}_3$  and  $\text{NaFe}_{1-x}\text{Mn}_x\text{F}_3$ ) in the entire compositional

range investigated (Figure 4 and Figure S2 (ESI)). No evidence of phase separation between the two end-members was present; there was no indication of long-range order for the transition metal cations in the mixed compositions. Figure S3 (ESI) shows the Rietveld refined XRPD patterns of the  $x = 0.5$  compositions as selected examples, demonstrating the good agreement between experimental and calculated patterns for the mixed cation compositions as well.

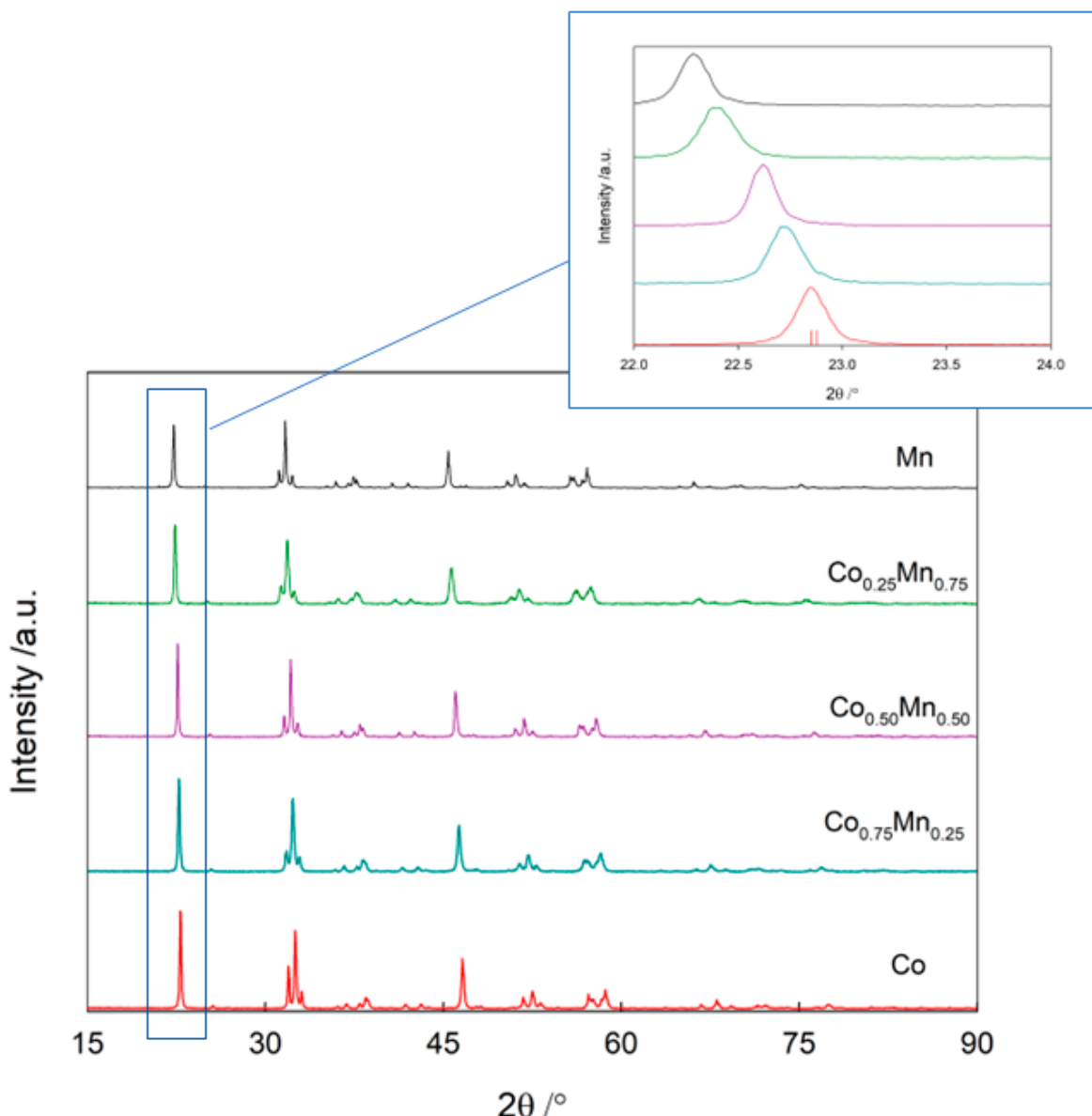


**Figure 4.** XRPD patterns of the  $\text{NaCo}_{1-x}\text{Mn}_x\text{F}_3$  series prepared without citric acid, highlighting the formation of a solid solution over the entire compositional range.

The unit cell volume vs. composition trends, reported in Figure 5a, showed that the cell volume varied almost linearly as a function of Mn content for both the systems as a result of a similar expansion for all the lattice parameters (Figure S4 (ESI)). These trends are consistent with the presence of  $M^{2+}$  cations in octahedral coordination considering their high spin configuration, as previously reported for  $\text{Fe}^{2+}$  in  $\text{NaFeF}_3$  [19]. In fact, according to the Shannon's ionic radii for octahedral coordination, the trend in ionic radii for high spin coordination follows the sequence of  $\text{Co}^{2+}(0.745 \text{ \AA}) < \text{Fe}^{2+}(0.78 \text{ \AA}) < \text{Mn}^{2+}(0.83 \text{ \AA})$ , while the same sequence would not justify the trend if considering the low spin configuration

( $\text{Fe}^{2+}(0.61 \text{ \AA}) < \text{Co}^{2+}(0.65 \text{ \AA}) < \text{Mn}^{2+}(0.67 \text{ \AA})$ ) [20]. In this way, apical and average equatorial M–F bond lengths increase linearly with the ionic radius (Figure 5b), as expected.

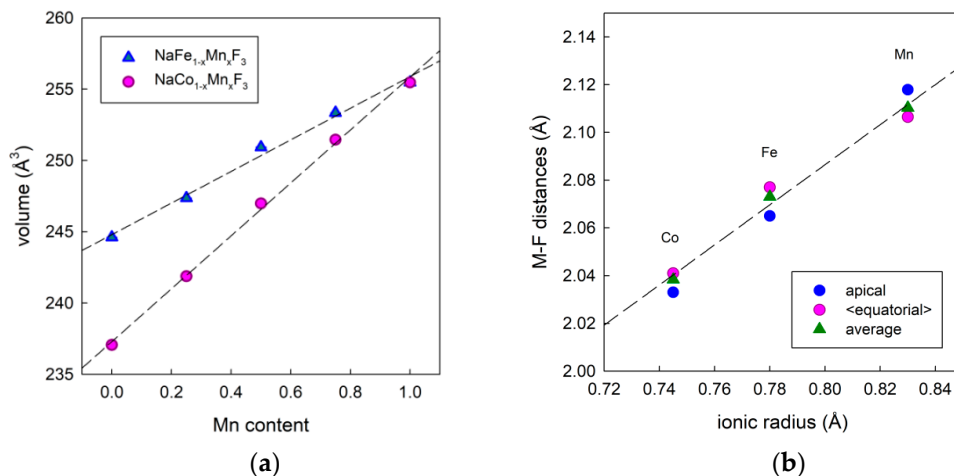


**Figure 5.** (a) Unit cell volume vs. composition for the two series, i.e.,  $\text{NaFe}_{1-x}\text{Mn}_x\text{F}_3$  and  $\text{NaCo}_{1-x}\text{Mn}_x\text{F}_3$ ; (b) M–F bond lengths vs. ionic radius for the three end-members  $\text{NaCoF}_3$ ,  $\text{NaFeF}_3$ , and  $\text{NaMnF}_3$ . Lines are linearly fit to the data, and error bars are within the size of the symbol.

Figure 6 shows the trend of the M–F–M tilting angle as a function of the ionic radius of the transition metal M, showing that the tilting angle deviated from the ideal value of  $180^\circ$ , following the sequence of Co, Fe, and Mn, with  $\text{NaMnF}_3$  being the more distorted composition. This trend was reproduced both for the apical and the equatorial bond angles, with minimum differences. Since in a small polaron system the hopping mechanism responsible for the electrical conductivity is favored when the hopping angle is close to  $180^\circ$  [21,22], based on the purely structural insight it is expected that the electronic contribution to conductivity in the series  $\text{NaMF}_3$  will be easier for the Co-containing sample compared to the case of  $\text{NaMnF}_3$ . Consistently, the calculated band gaps for the  $\text{NaMF}_3$  ( $M = \text{Co, Fe, and Mn}$ ) compositions according to the Materials Project Database [23] were 2.069, 2.748, and 3.010 eV for  $\text{NaCoF}_3$ ,  $\text{NaFeF}_3$ , and  $\text{NaMnF}_3$ , respectively, also suggesting electrical conductivities in the order of  $\text{NaCoF}_3 > \text{NaFeF}_3 > \text{NaMnF}_3$ .

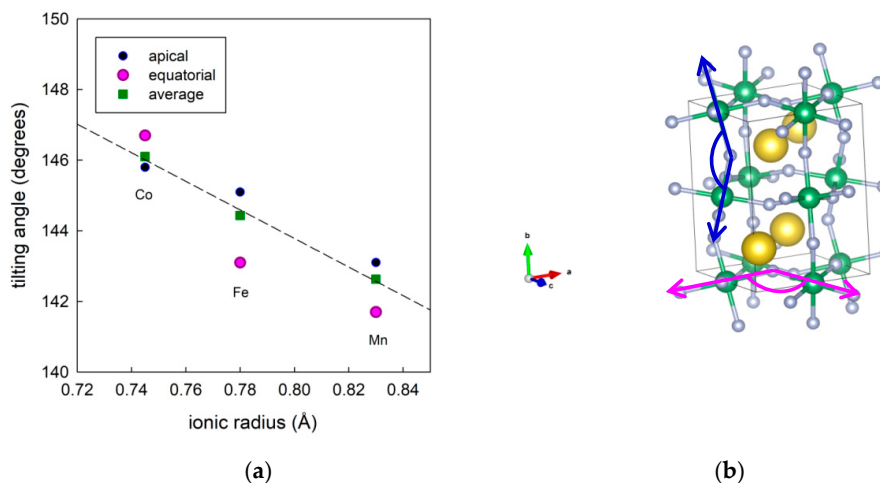


**Figure 6.** (a) F–M–F tilting angle vs. ionic radius for the three end-members  $\text{NaCoF}_3$ ,  $\text{NaFeF}_3$ , and  $\text{NaMnF}_3$ . Lines are linearly fit to the data, and error bars are within the size of the symbol; (b) schematic representation of the apical (blue) and equatorial (purple) tilting angles. Legend: Na is indicated in yellow; M is indicated in green; F is indicated in grey.

It is expected that the formation of solid solutions within the  $\text{NaCo}_{1-x}\text{Mn}_x\text{F}_3$  and  $\text{NaFe}_{1-x}\text{Mn}_x\text{F}_3$  systems will allow modulating the electrical conductivity as well as the intercalation voltage of these compounds, with values generated between those of the end-members following the structural modifications induced by composition.

The same compositions presented up to now were prepared using a modified synthesis, including the addition of sodium citrate, to modulate the average particles' size dimension and aggregation state. Figure 7a shows the comparison among the XRPD patterns of the  $\text{NaMnF}_3$  composition, selected as an example, prepared with different amounts of sodium citrate in the reaction mixture. All the samples were single-phase, with the same structure described above; however, the addition of sodium citrate broadened the diffraction profile, suggesting the presence of smaller particles in the sample. This was confirmed by the SEM characterization reported in Figure 7b,c, showing the comparison between the morphologies of the  $\text{NaMnF}_3$  and  $\text{NaCoF}_3$  samples, prepared with and without sodium citrate. In general, finer and more dispersed nano-sized particles were present in the sample prepared with sodium citrate, and this is expected to be beneficial for the intercalation properties of cathode materials.

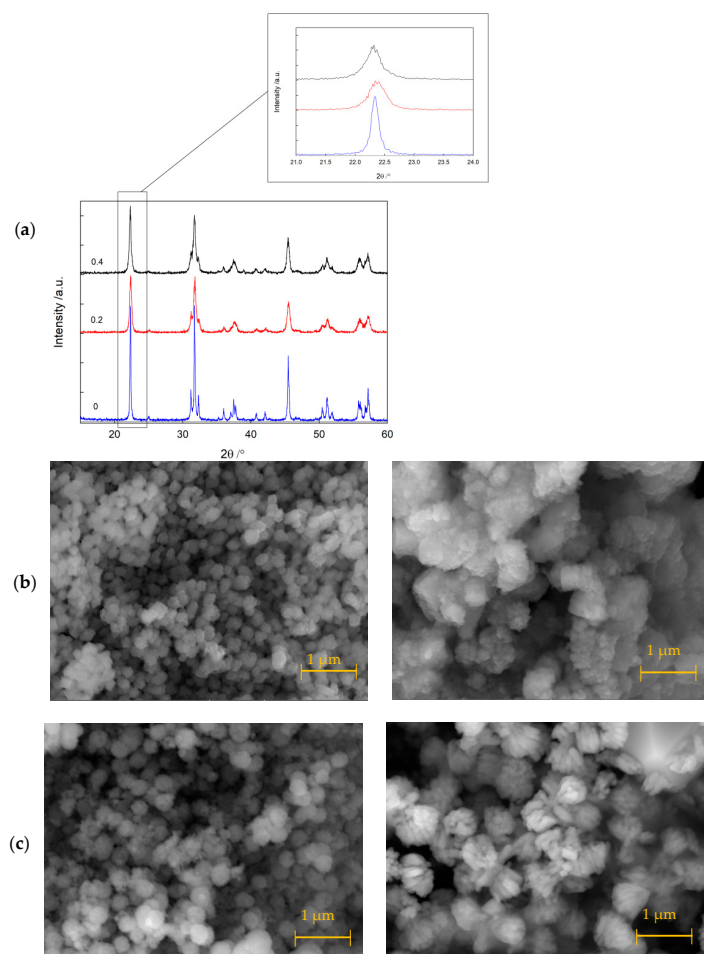


**Figure 7.** (a) XRPD patterns of  $\text{NaMnF}_3$  prepared with different amounts of sodium citrate (0 g; 0.2 g; 0.4 g), showing the broadening of the diffraction peaks when sodium citrate was present in the reaction mixture. (b) SEM images of the  $\text{NaMnF}_3$  compound prepared with (left) and without (right) sodium citrate; (c) SEM images of the  $\text{NaCoF}_3$  compound prepared with (left) and without (right) sodium citrate.

### 3.2. Materials Modelling

A good cathode material should possess both high electronic and ionic conductivity; ionic diffusion is crucial to ensure intercalation and deintercalation of the Na ion in the system, on the basis of the electrochemical process required for a cathode material in a rechargeable battery. Based on the pair-potential model reported in Table S2 (ESI) and the structural data obtained by Rietveld refinement (Table S1 (ESI)), the structural features of the three  $\text{NaCoF}_3$ ,  $\text{NaFeF}_3$ , and  $\text{NaMnF}_3$  compositions were reproduced with accuracy, as differences between the experimental and calculated lattice parameters were all below 0.08 Å. Table S3 (ESI) shows a direct comparison of these data.

The accurate reproduction of the experimental structural data with the use of the potential model was the basis for the subsequent defect calculations. Calculations were primarily used to extract information on the mechanism and energetics of Na ion diffusion in this family of materials. In particular, the energy barriers ( $E_a$ ) for Na ion diffusion through vacancy hopping along the paths schematically presented in Figure 8 were calculated and compared for the three compositions (Table 1). Paths A1 and A2 are related to the diffusion within the  $ac$  plane, the difference being the hopping distance between adjacent Na crystallographic sites; path B is related to the diffusion along the  $b$  axis. As shown in Table 1, path A2 and path B have very similar calculated migration barriers for all the three compositions, while path A1 is characterized by a slightly higher value. These results suggested that Na ion diffusion in  $\text{NaMF}_3$  will likely proceed through a 3D path, involving both the  $ac$  plane and the  $b$  direction. In general, the trend in calculated values suggested that Na ion diffusivity will follow the order of  $\text{NaMnF}_3 > \text{NaFeF}_3 > \text{NaCoF}_3$ . This trend showed a very good correlation with the experimental volume of the Na–F coordination polyhedron along with the composition derived from the crystallographic data in this study and reported in Figure 9a: the higher the volume, the lower the migration barrier and, therefore, the easier the migration of the Na-ion within the structure. An even better correlation can be found for the trend in the activation barrier along with the average Na–F distance at the saddle point configuration (Figure 9b), which is an estimate of the steric hindrance to Na ion diffusion in the strcuture. Figure 9 shows that changes in activation barriers for Na ion migration can be related to key structural parameters that are a function of the ionic radius of the transition metal in  $\text{NaCoF}_3$ ,  $\text{NaFeF}_3$ , and  $\text{NaMnF}_3$ . Figure S5 (ESI) shows that such structural parameters changed linearly with the compositions in the two solid solutions, i.e.,  $\text{NaCo}_{1-x}\text{Mn}_x\text{F}_3$  and  $\text{NaFe}_{1-x}\text{Mn}_x\text{F}_3$ . As explained in Section 2, the computational investigation was carried on the three end-members and not on all the mixed metal compositions; however, the structural correlations found in this study suggest that the activation barrier for Na ion diffusion in the systems under investigation will decrease along with the Mn content (i.e., as the average Na–F at the saddle point configuration increases).

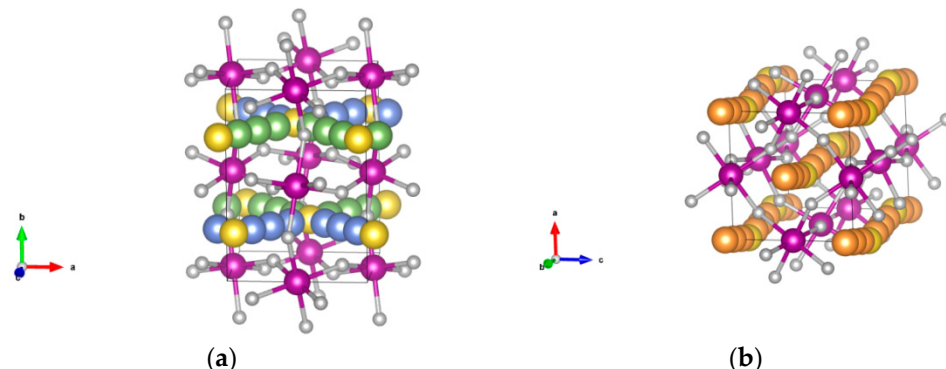


**Figure 8.** Schematic representation of the Na-ion migration paths for  $\text{NaMnF}_3$ : (a) path A1 in green and path A2 in blue; (b) path B in orange. Legend: Na is indicated in yellow; Mn is indicated in purple; F is indicated in grey.

**Table 1.** Calculated activation energies ( $E_a$ ) for Na-ion diffusion in the  $\text{NaMF}_3$  system ( $M = \text{Co}, \text{Fe}$ , and  $\text{Mn}$ ), according to the paths presented in Figure 8.

	$E_a$ (eV)		
	$\text{NaCoF}_3$	$\text{NaFeF}_3$	$\text{NaMnF}_3$
Path A1	1.27	1.24	1.21
Path A2	1.11	1.06	1.00
Path B	1.14	1.08	1.01

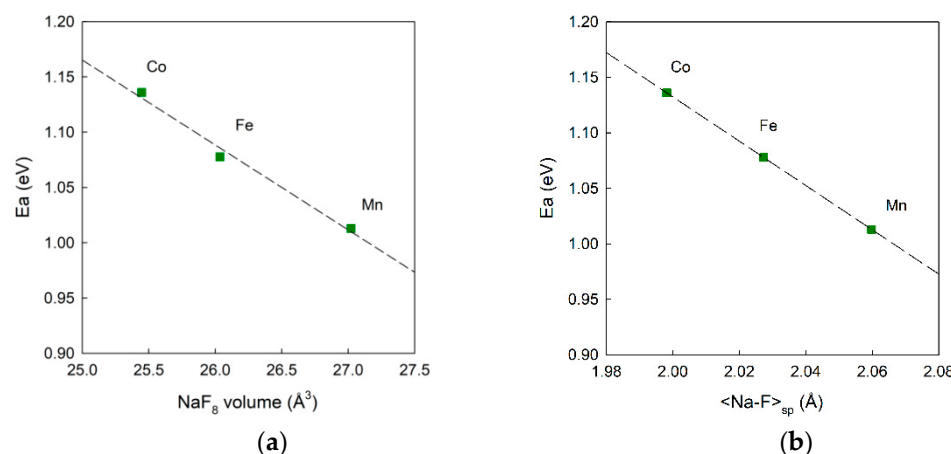


**Figure 9.** (a) Na-ion migration barrier ( $E_a$ ) for path B as a function of the Na–F coordination polyhedral volume for  $\text{NaMF}_3$  ( $M = \text{Co}, \text{Fe}$ , and  $\text{Mn}$ ); (b) Na-ion migration barrier ( $E_a$ ) for path B as a function of the average Na–F distance at the saddle point configuration for  $\text{NaMF}_3$  ( $M = \text{Co}, \text{Fe}$ , and  $\text{Mn}$ ).  $E_a$  was calculated, and volumes were experimentally derived values in this study. The dashed line is the linear interpolation of the data.

It should be recognized that the calculated migration barrier for Na-ion diffusion of approximately 1 eV is considered relatively high for good cathode materials [24], and nanosizing is expected to improve the rate capabilities of cathode materials presenting high migration barriers for ionic diffusion. This might, therefore, be one of the reasons at the basis of the better electrochemical performances found for  $\text{NaFeF}_3$  fine and dispersed nanosized samples compared to micrometer samples, especially at high C rates [6].

The defect structure underlies the functional properties of materials. In particular, there are very well-known examples of the effect of point defects on the intercalation properties of batteries' cathode materials, e.g., anti-site defects in olivine-type cathodes [25,26] and inversion degree in spinel-type cathodes [27,28]. Such defects are due to the substitution of the diffusing alkali ion and the transition metal ion in their respective sites, which could have a strong impact on the intercalation properties of the cathode, should the defect block preferential diffusion paths for the alkali ion. The formation energies for antisite defects in this structure were calculated for isolated and cluster defects according to the following equation (Kroger–Vink notation):



The difference between the calculated energies for the formation of clustered and isolated anti-site defects is the binding energy, and according to this notation, negative values imply that the two charged defects are bound, i.e., they tend to aggregate, thus impeding Na-ion diffusion. The calculated results are compared in Table 2 and showed that the formation of this kind of defect was favorable; for comparison, the calculated formation energy of the clustered anti-site defect in the  $\text{LiFePO}_4$  olivine cathode was 0.74 eV [26], and this is known to highly affect the intercalation properties of the material [25,29,30]. As for

the olivine system, the anti-site defects in  $\text{NaMF}_3$ , if present, will be bound, as the binding energies values are favorable. The results in Table 2 also suggested a trend in the formation and binding of these defects along with composition, with the lower formation energy identified for the Mn-containing compound.

**Table 2.** Calculated formation energies for isolated and clustered anti-site defects in  $\text{NaMF}_3$  ( $M = \text{Co}$ ,  $\text{Fe}$ , and  $\text{Mn}$ ).

	$\text{NaCoF}_3$	$\text{NaFeF}_3$	$\text{NaMnF}_3$
Anti-site isolated (eV)	1.62	1.42	1.19
Anti-site cluster (eV)	0.86	0.71	0.55
Binding energy (eV)	−0.76	−0.71	−0.64

It should be noted that, although anti-site defects might be present in the perovskite structure, especially if high-temperature treatments are used for their preparation, the prediction of a mainly 3D diffusion path compared to the strict 1D diffusion path of the olivine phase suggests that the detrimental effect of their presence on the intercalation properties of the cathode will be limited.

#### 4. Conclusions

Transition metal fluoride perovskites are potential cathode materials for Na-ion rechargeable batteries. In particular, previous studies have proven the reversibility of Na intercalation in  $\text{NaFeF}_3$  and suggested that high-voltage cathode materials in this family of compounds could be  $\text{NaMnF}_3$  and, in particular,  $\text{NaCoF}_3$ , with a predicted average intercalation voltage higher than 4.6 V. Major problems in the application of these materials are related to low conductivities and high intercalating voltages compared to the stability windows of available electrolytes for Na ion batteries.

In this study, we combined experimental and computational techniques and found clear correlations among experimentally derived structural features and calculated transport properties, investigating for the first time the preparation of mixed metal compositions in the Fe/Mn and Co/Mn systems and the mechanisms and energetics of Na ion diffusion in this structure.

The XRPD characterization of the samples revealed that the proposed synthesis, transferred from the preparation of  $\text{NaCoF}_3$ , was able to produce all the compositions investigated as single-phase, showing the formation of two solid solutions with a perovskite structure for the  $\text{NaFe}_{1-x}\text{Mn}_x\text{F}_3$  and  $\text{NaCo}_{1-x}\text{Mn}_x\text{F}_3$  systems. This simple solvothermal process uses green and relatively inexpensive precursors, and it is easily scalable to high amounts of samples. In comparison to the most common solid-state and mechanochemical syntheses, it requires low thermal treatments, and it is expected to produce carbon-coated nanosized samples that could be tested as high-voltage cathode materials for NIBs.

Na ion intercalation in these compounds is predicted to follow a three-dimensional path, thus limiting the potential negative effect of the presence of anti-site defects in the structure. The calculated energy barriers for Na ion diffusion were relatively high, suggesting that ion diffusion may be a limiting step in the application of this family of materials as intercalation cathodes for NIBs. Nanostructuring is expected to improve the electrochemical performances of this family of cathode materials.

Based on structural and computational data, this study suggests that the conductivity (both electronic and ionic) in mixed metal perovskite-type fluorides could be finely tuned through compositional changes, thus providing designing rules for the preparation of cathode materials with targeted properties.

**Supplementary Materials:** The following supporting information can be downloaded at: <https://www.mdpi.com/article/10.3390/batteries8090126/s1>; Figure S1: XRPD patterns of  $\text{NaFeF}_3$  prepared in air and in Ar-filled glove box; Figure S2: XRPD patterns of the  $\text{NaMn}_{1-x}\text{Fe}_x\text{F}_3$  series prepared without sodium citrate; Figure S3: Rietveld refined XRPD patterns of the  $\text{NaMn}_{0.5}\text{Fe}_{0.5}\text{F}_3$

and the  $\text{NaMn}_{0.5}\text{Co}_{0.5}\text{F}_3$  compounds prepared without sodium citrate; Figure S4: Lattice parameters vs composition trend for  $\text{NaFe}_{1-x}\text{Mn}_x\text{F}_3$  and  $\text{NaCo}_{1-x}\text{Mn}_x\text{F}_3$ ; Figure S5: Average Na-F distance at the saddle point configuration as a function of the Mn content for  $\text{NaFe}_{1-x}\text{Mn}_x\text{F}_3$  and  $\text{NaCo}_{1-x}\text{Mn}_x\text{F}_3$ ; Table S1: Rietveld refined structural parameters; Table S2: Pair potential (Buckingham functional) and shell model parameters; Table S3: Comparison between calculated and experimental structural parameters.

**Author Contributions:** Conceptualization, C.T.; methodology, M.M. and C.T.; investigation, M.M., D.C., U.A.T. and C.T.; writing—original draft preparation, C.T.; writing—review and editing, C.T. and U.A.T.; supervision, C.T.; funding acquisition, C.T. All authors have read and agreed to the published version of the manuscript.

**Funding:** Financial support by Fondazione Cariplo-Regione Lombardia through grant 2015-0753 is gratefully acknowledged.

**Data Availability Statement:** The data presented in this study are available, upon reasonable request, from the corresponding author.

**Conflicts of Interest:** The authors declare no conflict of interest.

## References

1. Delmas, C. Sodium and Sodium-Ion Batteries: 50 Years of Research. *Adv. Energy Mater.* **2018**, *8*, 1703137. [[CrossRef](#)]
2. Goikolea, E.; Palomares, V.; Wang, S.; de Larramendi, I.R.; Guo, X.; Wang, G.; Rojo, T. Na-Ion Batteries—Approaching Old and New Challenges. *Adv. Energy Mater.* **2020**, *10*, 2002055. [[CrossRef](#)]
3. You, Y.; Manthiram, A. Progress in High-Voltage Cathode Materials for Rechargeable Sodium-Ion Batteries. *Adv. Energy Mater.* **2018**, *8*, 1701785. [[CrossRef](#)]
4. Li, Y.; Lu, Y.; Zhao, C.; Hu, Y.S.; Titirici, M.M.; Li, H.; Huang, X.; Chen, L. Recent Advances of Electrode Materials for Low-Cost Sodium-Ion Batteries towards Practical Application for Grid Energy Storage. *Energy Storage Mater.* **2017**, *7*, 130–151. [[CrossRef](#)]
5. Kitajou, A.; Ishado, Y.; Yamashita, T.; Momida, H.; Oguchi, T.; Okada, S. Cathode Properties of Perovskite-Type  $\text{NaMF}_3$  ( $M = \text{Fe}$ ,  $\text{Mn}$ , and  $\text{Co}$ ) Prepared by Mechanical Ball Milling for Sodium-Ion Battery. *Electrochim. Acta* **2017**, *245*, 424–429. [[CrossRef](#)]
6. Yamada, Y.; Doi, T.; Tanaka, I.; Okada, S.; Yamaki, J.I. Liquid-Phase Synthesis of Highly Dispersed  $\text{NaFeF}_3$  Particles and Their Electrochemical Properties for Sodium-Ion Batteries. *J. Power Sources* **2011**, *196*, 4837–4841. [[CrossRef](#)]
7. Nava-Avendaño, J.; Arroyo-De Dompablo, M.E.; Frontera, C.; Ayllón, J.A.; Palacín, M.R. Study of Sodium Manganese Fluorides as Positive Electrodes for Na-Ion Batteries. *Solid State Ionics* **2015**, *278*, 106–113. [[CrossRef](#)]
8. Kitajou, A.; Komatsu, H.; Chihara, K.; Gocheva, I.D.; Okada, S.; Yamaki, J.I. Novel Synthesis and Electrochemical Properties of Perovskite-Type  $\text{NaFeF}_3$  for a Sodium-Ion Battery. *J. Power Sources* **2012**, *198*, 389–392. [[CrossRef](#)]
9. Kravchyk, K.V.; Zünd, T.; Wörle, M.; Kovalenko, M.V.; Bodnarchuk, M.I.  $\text{NaFeF}_3$  Nanoplates as Low-Cost Sodium and Lithium Cathode Materials for Stationary Energy Storage. *Chem. Mater.* **2018**, *30*, 1825–1829. [[CrossRef](#)]
10. Yuan, L.X.; Wang, Z.H.; Zhang, W.X.; Hu, X.L.; Chen, J.T.; Huang, Y.H.; Goodenough, J.B. Development and Challenges of  $\text{LiFePO}_4$  Cathode Material for Lithium-Ion Batteries. *Energy Environ. Sci.* **2011**, *4*, 269–284. [[CrossRef](#)]
11. Chun, J.; Jo, C.; Lim, E.; Roh, K.C.; Lee, J. Solvothermal Synthesis of Sodium Cobalt Fluoride ( $\text{NaCoF}_3$ ) Nanoparticle Clusters. *Mater. Lett.* **2017**, *207*, 89–92. [[CrossRef](#)]
12. Rodriguez-Carvajal, J. Recent Advances in Magnetic Structure Determination by Neutron Powder Diffraction. *Phys. B* **1993**, *192*, 55–69. [[CrossRef](#)]
13. Lutgert, B.; Babel, D. Kristallstrukturverfeinerungen an Natriumtrifluorometallaten  $\text{NaMF}_3$  ( $M = \text{Mg}$ ,  $\text{Co}$ ,  $\text{Ni}$ ,  $\text{Zn}$ ): Oktaederkipfung Und Toleranzfaktor Orthorhombischer Fluorperowskite. *Zeitschrift Anorg. Allg. Chem.* **1992**, *616*, 133–140. [[CrossRef](#)]
14. Gale, J.D.; Rohl, A.L. The General Utility Lattice Program (GULP). *Mol. Simul.* **2003**, *29*, 291–341. [[CrossRef](#)]
15. Gale, J.D. GULP: A Computer Program for the Symmetry-Adapted Simulation of Solids. *J. Chem. Soc. Faraday Trans.* **1997**, *93*, 148, 629–637. [[CrossRef](#)]
16. Tripathi, R.; Wood, S.M.; Islam, M.S.; Nazar, L.F. Na-Ion Mobility in Layered  $\text{Na}_2\text{FePO}_4\text{F}$  and Olivine  $\text{Na}[\text{Fe},\text{Mn}]\text{PO}_4$ . *Energy Environ. Sci.* **2013**, *6*, 2257–2264. [[CrossRef](#)]
17. Dick, B.G.; Overhauser, A.W. Theory of the Dielectric Constants of Alkali Halide Crystals. *Phys. Rev.* **1958**, *112*, 90–103. [[CrossRef](#)]
18. Mott, N.F.; Littleton, M.J. Conduction in polar crystals. Solid, I. Electrolytic conduction in salt. *Trans. Faraday Soc.* **1938**, *34*, 485–499. [[CrossRef](#)]
19. Bernal, F.L.; Yusenko, K.V.; Sottmann, J.; Drathen, C.; Guignard, J.; Løvvik, O.M.; Crichton, W.A.; Margadonna, S. Perovskite to Postperovskite Transition in  $\text{NaFeF}_3$ . *Inorg. Chem.* **2014**, *53*, 12205–12214. [[CrossRef](#)]
20. Shannon, R.D. Revised Effective Ionic Radii and Systematic Studies of Interatomic Distances in Halides and Chalcogenides. *Acta Crystallogr. Sect. A* **1976**, *32*, 751–767. [[CrossRef](#)]
21. Tealdi, C.; Malavasi, L.; Gozzo, F.; Ritter, C.; Mozzati, M.C.; Chiodelli, G.; Flor, G. Correlation between Transport Properties and Lattice Effects in the  $\text{NdCoO}_3$ -Based Catalysts and Sensor Materials. *Chem. Mater.* **2007**, *19*, 4741–4750. [[CrossRef](#)]

22. Khan, W.; Naqvi, A.H.; Gupta, M.; Husain, S.; Kumar, R. Small Polaron Hopping Conduction Mechanism in Fe Doped LaMnO<sub>3</sub>. *J. Chem. Phys.* **2011**, *135*, 054501. [[CrossRef](#)] [[PubMed](#)]
23. Jain, A.; Ong, S.P.; Hautier, G.; Chen, W.; Richards, W.D.; Dacek, S.; Cholia, S.; Gunter, D.; Skinner, D.; Ceder, G.; et al. Commentary: The Materials Project: A Materials Genome Approach to Accelerating Materials Innovation. *APL Mater.* **2013**, *1*, 011002. [[CrossRef](#)]
24. Rong, Z.; Malik, R.; Canepa, P.; Gautam, G.S.; Liu, M.; Jain, A.; Persson, K.; Ceder, G. Materials Design Rules for Multivalent Ion Mobility in Intercalation Structures. *Chem. Mater.* **2015**, *27*, 6016–6021. [[CrossRef](#)]
25. Park, K.Y.; Park, I.; Kim, H.; Lim, H.D.; Hong, J.; Kim, J.; Kang, K. Anti-Site Reordering in LiFePO<sub>4</sub>: Defect Annihilation on Charge Carrier Injection. *Chem. Mater.* **2014**, *26*, 5345–5351. [[CrossRef](#)]
26. Islam, M.S.; Driscoll, D.J.; Fisher CA, J.; Slater, P.R. Atomic-Scale Investigation of Defects, Dopants, and Lithium Transport in the LiFePO<sub>4</sub> Olivine-Type Battery Material. *Chem. Mater.* **2005**, *17*, 5085–5092. [[CrossRef](#)]
27. Gautam, G.S.; Canepa, P.; Urban, A.; Bo, S.; Ceder, G. Influence of Inversion on Mg Mobility and Electrochemistry in Spinel. *Chem. Mater.* **2017**, *29*, 7918–7930. [[CrossRef](#)]
28. Morando, C.; Cofrancesco, P.; Tealdi, C. Zn Ion Diffusion in Spinel-Type Cathode Materials for Rechargeable Batteries: The Role of Point Defects. *Mater. Today Commun.* **2020**, *25*, 101478. [[CrossRef](#)]
29. Tealdi, C.; Spreafico, C.; Mustarelli, P. Lithium Diffusion in Li<sub>1-x</sub>FePO<sub>4</sub>: The Effect of Cationic Disorder. *J. Mater. Chem.* **2012**, *22*, 24870. [[CrossRef](#)]
30. Chen, J.; Graetz, J. Study of Antisite Defects in Hydrothermally Prepared LiFePO<sub>4</sub> by in Situ X-ray Diffraction. *ACS Appl. Mater. Interfaces* **2011**, *3*, 1380–1384. [[CrossRef](#)]